



Article

Thin-Film Lithium Niobate Based Acousto-Optic Modulation Working at Higher-Order TE₁ Mode

Yang Yang¹, Yin Xu^{1,*} , Dongmei Huang^{2,3}, Feng Li³, Yue Dong¹ , Bo Zhang¹, Yi Ni¹ and P. K. A. Wai^{3,4}

¹ Department of Electronic Engineering, School of IoT Engineering, Jiangnan University, Wuxi 214122, China; yangyang@stu.jiangnan.edu.cn (Y.Y.); y.dong@jiangnan.edu.cn (Y.D.); zhangb2018@jiangnan.edu.cn (B.Z.); 8073110160@jiangnan.edu.cn (Y.N.)

² Photonics Research Center, Department of Electrical Engineering, The Hong Kong Polytechnic University, Hong Kong, China; meihk.huang@polyu.edu.hk

³ The Hong Kong Polytechnic University Shenzhen Research Institute, Shenzhen 518057, China; enlf@polyu.edu.hk (F.L.); alexwai@hkbu.edu.hk (P.K.A.W.)

⁴ Department of Physics, Hong Kong Baptist University, Hong Kong, China

* Correspondence: yin.xu@jiangnan.edu.cn

Abstract: Acousto-optic modulation (AOM) is regarded as an effective way to link multi-physical fields on-chip. We propose an on-chip AOM scheme based on the thin-film lithium niobate (TFLN) platform working at the higher-order TE₁ mode, rather than the commonly used fundamental TE₀ mode. Multi-physical field coupling analyses were carried out to obtain the refractive index change of the optical waveguide ($>6.5 \times 10^{-10}$ for a single phonon) induced by the enhanced acousto-optic interaction between the acoustic resonator mode and the multimode optical waveguide. By using a Mach-Zehnder interferometer (MZI) structure, the refractive index change is utilized to modulate the output spectrum of the MZI, thus achieving the AOM function. In the proposed AOM scheme, efficient mode conversion between the TE₀ and TE₁ mode is required in order to ensure that the AOM works at the higher-order TE₁ mode in the MZI structure. Our results show that the half-wave-voltage-length product ($V_{\pi}L$) is <0.01 V·cm, which is lower than that in some previous reports on AOM and electro-optic modulation (EOM) working at the fundamental TE₀ mode (e.g., $V_{\pi}L > 0.04$ V·cm for AOM, $V_{\pi}L > 1$ V·cm for EOM). Finally, the proposed AOM has lower loss when compared with EOM because the electrode of the AOM can be placed far from the optical waveguide.

Keywords: acousto-optic modulation; thin-film lithium niobate; photonic integrated components



Citation: Yang, Y.; Xu, Y.; Huang, D.; Li, F.; Dong, Y.; Zhang, B.; Ni, Y.; Wai, P.K.A. Thin-Film Lithium Niobate Based Acousto-Optic Modulation Working at Higher-Order TE₁ Mode. *Photonics* **2022**, *9*, 12. <https://doi.org/10.3390/photonics9010012>

Received: 29 November 2021

Accepted: 23 December 2021

Published: 28 December 2021

Publisher's Note: MDPI stays neutral with regard to jurisdictional claims in published maps and institutional affiliations.



Copyright: © 2021 by the authors. Licensee MDPI, Basel, Switzerland. This article is an open access article distributed under the terms and conditions of the Creative Commons Attribution (CC BY) license (<https://creativecommons.org/licenses/by/4.0/>).

1. Introduction

Acousto-optic modulation (AOM) connecting the electric, mechanical, and optical fields, takes a vital role in the microwave, lightwave, and quantum photonic signal processing [1–5]. Comparing with integrated electro-optic modulations (EOMs) [6–10], AOM typically works with multiple physical fields and its basic working process can be described as follows. Firstly, the input microwave signal is converted to the acoustic wave transmitted along the acoustic medium through a piezoelectric transducer (e.g., interdigital transducer (IDT)). Secondly, the generated acoustic wave would interact with the optical mode of the waveguide, leading to a change in the mode effective index of the optical waveguide. Finally, the mode effective index change is used to modulate the output spectrum via waveguide structures, such as a Mach-Zehnder interferometer (MZI) [1,3] or microring resonator (MRR) [1,4]. On-chip integrated AOM can enhance the AOM performance and reduce the device dimension, but requires an ideal material platform to ensure efficient couplings between the different physical fields.

Recently, various materials such as aluminum nitride (AlN) [11,12], gallium arsenide (GaAs) [13,14], gallium phosphide (GaP) [15,16], silicon [17,18], and lithium niobate

(LN) [19,20] have been adopted for AOM. Among them, LN is the most promising candidate especially for the thin-film LN (TFLN) or LN-on-insulator (LNOI) owing to its wide transparent window (from 400 nm to 5 μm), high refractive index contrast ($\Delta n > 0.7$), large piezoelectric, electro-optic, photo-elastic, and nonlinear coefficients, as well as stable physical and chemical properties [1,19–24]. Thus, integrated AOM based on the TFLN platform will have compact size and high integration density together with dramatically enhanced acousto-optic interaction (AOI). For example, in 2019, Cai et al. demonstrated the first TFLN-based AOM [25]. Both MZI-type and high-Q MRR-type modulators were fabricated on the same chip. Strong optical field enhancement and interaction were achieved when compared with conventional bulk LN or other material platforms (e.g., GaAs [13,14]). The maximum microwave modulation frequency and the key half-wave-voltage-length product ($V_{\pi}L$) were 111.725 MHz and 5 V·cm, respectively, for the MZI-type AOM. A high Q (>300,000) optical resonator was realized with stronger amplitude modulation for the MRR-type AOM [25]. To further enhance the AOI and improve the modulation frequency, Shao et al. used a suspended TFLN to construct an acoustic resonator and leveraged the triple resonance among the electric, mechanical, and optical fields to greatly enhance the microwave-to-optical conversion. Microwave modulation frequency up to 4.5 GHz and $V_{\pi}L$ down to 0.046 V·cm were demonstrated. The Q factor is $>2 \times 10^6$ for the MRR-type AOM [26]. Note that such an ultra-low $V_{\pi}L$ value is quite useful for on-chip low power and low-loss modulation. Such performance cannot be easily achieved by current TFLN-based EOMs (best value ~ 1.0 V·cm [27–29]). For the EOMs, the modulation electrodes need to be placed as close to the optical waveguide as possible in order to effectively reduce the driving voltage, at the cost of increased metal absorption loss. For the AOM, as it is the generated acoustic wave that interacts with the optical mode, the modulation electrodes can be placed far from the optical waveguide. Thus, the electrode absorption loss is almost negligible. Since it is difficult to achieve high-quality etching of TFLN, etchless TFLN platform has been considered, in which the optical waveguides were formed by patterning other materials (e.g., Si [30], Si_3N_4 [31], polymer [32]) atop the etchless TFLN wafer. Based upon such a scheme, etchless TFLN-based AOM has been realized with modulation frequency beyond 4 GHz and Q factor higher than 500,000 [32].

Optomechanical crystals are typically used to achieve the piezo-optomechanical modulation in applications from sensing to quantum information science [33–35]. The inefficient electromechanical coupling because of the mode mismatch between different physical fields is the main challenge to be overcome. The key issues in the reported AOM schemes are to improve the conversion efficiency from the microwave input to the acoustic resonator mode and to enhance the AOI. Moreover, we note that, at present, the fundamental optical mode is the only optical mode used for the AOI. In view of the acoustic wave distribution and the size at the TFLN platform, higher-order optical mode (such as TE_1 mode) should bring out a stronger AOI if it is used as the working optical mode. The performance of on-chip AOM should also improve.

In this paper, we propose an on-chip AOM based on a 600 nm-thick X-cut TFLN working at the higher-order TE_1 mode rather than the commonly used fundamental TE_0 mode. The proposed AOM structure was designed, analyzed, and optimized in detail for the TE_1 mode to achieve stronger AOI when compared with that for the TE_0 mode. Multi-physical field analyses were carried out to acquire the different mode field interactions. We then embedded the proposed AOM structure in a typical MZI circuit to construct an MZI-type AOM, in which an efficient mode converter from the TE_0 to TE_1 mode and vice versa was also designed. From our calculation, the total refractive index change for the optical multimode waveguide is larger than 6.5×10^{-10} (for a single phonon). The photo-elastic effect, moving boundary effect, and electro-optic effect were all included in the analysis of the AOI effect. The key $V_{\pi}L$ is reduced to less than 0.01 V·cm, which is superior to those AOMs working at the fundamental TE_0 mode and other EOMs, (e.g., $V_{\pi}L > 0.04$ V·cm for AOM, $V_{\pi}L > 1$ V·cm for EOM) [25–29]. Moreover, the metal absorption loss of the proposed AOM is quite low, since the key modulation electrodes of the AOM do not need

to be placed close to the optical waveguide, while close electrode placement to the optical waveguide is necessary for EOM. The proposed AOM scheme would contribute to the development of on-chip low power, low loss, and compact AOM. AOM-related applications and components, such as frequency shifter [1,5], tunable filter [1,5], beamforming [3], and cavity optomechanics [33–35] would also be benefited, contributing to the building of on-chip photonic systems.

2. Materials and Methods

Figure 1a shows the schematic layout of the proposed AOM working at the higher-order TE_1 mode. The key modulation part is integrated at one arm of the MZI structure together with the mode converters. The whole device is based on a 600 nm-thick X-cut TFLN. Owing to the excellent piezoelectric properties of TFLN, energy conversion from the applied microwave electric field to surface acoustic wave (SAW) can be realized with the use of IDT [12,14,25,26,32,33,35]. Accordingly, we choose the electrode parameters of the IDT to match with the wavelength of the SAW and deposit the IDT on the surface of the TFLN directly (parallel to the optical waveguide). For the generated SAW, it will transmit along the TFLN and further interact with the optical mode, where the propagation directions of the SAW and optical wave are perpendicular with each other. To enhance the AOI effect, we use the higher-order TE_1 mode as the working optical mode (the two mode spots have a π phase difference between them) within the waveguide region. As a result, the optical refractive index change of the TFLN optical waveguide is effectively increased when compared with that of AOM working at the fundamental TE_0 mode. The relatively large optical refractive index change can be utilized to modulate the output spectrum by using an optical MZI structure. This is the key idea of the present work. Figure 1b plots the cross-sectional view of the AOM along the x - z direction, where the waveguide width and etching depth are w and h_1 ($=300$ nm), respectively, and the electrode width, gap and thickness of IDT are a ($=300$ nm), b ($=300$ nm) and 100 nm, respectively. The gap width between the optical waveguide and IDT is G . Moreover, the gap width between the IDT and the left side of the acoustic resonator is chosen as L_t ($=1.2$ μ m), to match with the wavelength of the generated SAW. Considering the current fabrication abilities, the slant angle of the TFLN waveguide sidewall is set to 70° for the proposed AOM design [3,19–24,26]. Note that we also etch two relatively large slots on both sides of the AOM along the y - z direction as shown in Figure 1a (light gray rectangular) to make the corrosive liquid contact with the buried oxide (BOX) layer below the AOM region and remove it via the corrosion method. As a result, the generated SAW is well-confined and transmitted in the top LN layer of the TFLN wafer and has stronger interaction with the optical waveguide when compared with some of the BOX unremoved schemes [5,25], which contributes to the on-chip low- $V_\pi L$ modulation. More important, the etched two slots form an acoustic resonator to enhance the SAW energy through the resonance effect [25,33–35]. The width of the acoustic resonator is set to 12 μ m. Figure 1c illustrates the enlarged view of the mode converters from the TE_0 mode to the TE_1 mode and vice versa, where the widths and gap of the two-coupled waveguides of the asymmetrical directional coupler are w_1 , w and d , respectively. The coupling length is L_C and the length between these two mode conversion regions is L_R . Using the proposed structure, the generated SAW and higher-order TE_1 mode interact well with each other within the modulation region, leading to the change of the optical refractive index of the TFLN waveguide, which will modulate the output spectrum of the MZI structure.

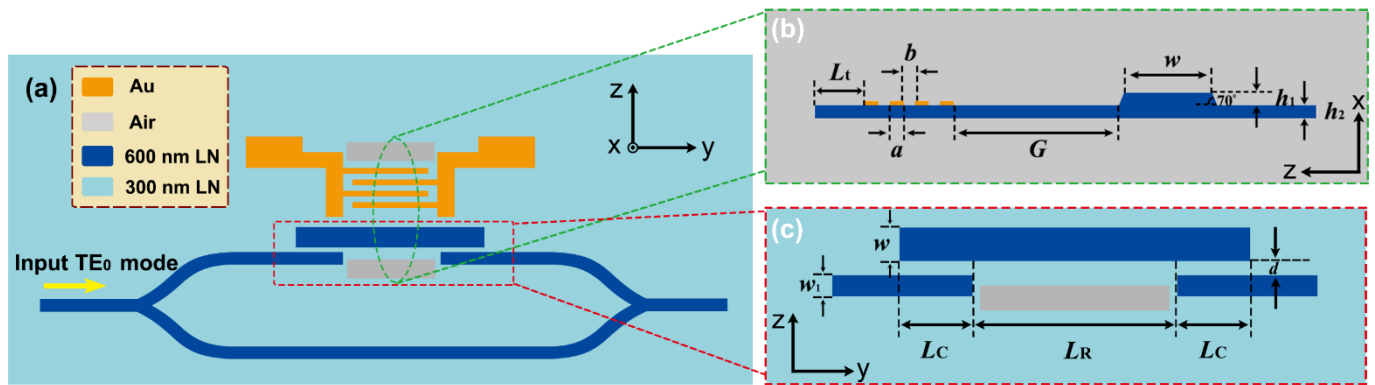


Figure 1. (a) Schematic of the proposed AOM working at the higher-order TE₁ mode based on a 600 nm-thick X-cut TFLN. The modulation region is located at one arm of the MZI structure and the other arm is used for reference. (b) Cross-sectional view of the AOM in the x - z direction. (c) Enlarged view of the mode conversion region. The structural materials and parameters are also labelled.

The multi-physical field effects acting on the overall AOI should be analyzed first before we optimize the structure of the AOM. In typical AOMs, the generated elastic wave (SAW) introduces the optomechanical coupling which leads to the structural distortion of the optical waveguide because of the photo-elastic effect and moving boundary effect of TFLN [36,37]. The structural distortion can also induce the generation of electric field through the piezoelectric effect of TFLN. The generated electric field will further affect the optical field based on the electro-optic effect of TFLN. Therefore, the overall modulation performance of the proposed on-chip AOM is determined by a combination of the moving boundary effect, photo-elastic effect, and electro-optic effect [26]. This combination effect will ultimately change the refractive index of the optical waveguide and modulate the output spectrum of the AOM embedded MZI structure.

The following theoretical analysis are based on the two-dimensional (2D) structure (x - z) of the AOM (along the SAW propagation direction), the results of which can be used to evaluate the coupling strength of the mode field interaction for the on-chip AOM. Firstly, the moving boundary effect due to the elastic deformation of the TFLN acting on the change of the refractive index of the optical waveguide is given by [26,36,37]

$$\Delta n_{MB} = -\frac{n}{2} \frac{\oint (Q \cdot \hat{n}) \left(E_{\parallel}^* \Delta \epsilon E_{\parallel} - D_{\perp}^* \Delta \epsilon^{-1} D_{\perp} \right) dS}{\int E^* \epsilon E dr} \chi_{zpf}, \quad (1)$$

where \hat{n} is the normal vector of the boundary facing outward, n is the optical refractive index along the z -direction of the TFLN, E is the electric field distribution, E_{\parallel} is the electric field component parallel to the interface, D_{\perp} is the electric displacement field component perpendicular to the interface, ϵ is the permittivity of the optical electric field, $\Delta \epsilon = \epsilon_{LN} - \epsilon_{air}$, and $\Delta \epsilon^{-1} = \epsilon_{LN}^{-1} - \epsilon_{air}^{-1}$, respectively. χ_{zpf} is the zero-point motion of the mechanical mode representing the coupling between the electromagnetic field and mechanical field ($\chi_{zpf} = \sqrt{\hbar/2m_{eff}\omega_m}$) [36], where ω_m is the resonant frequency of the acoustic mode and \hbar is the reduced Planck constant. S defines the 2D simulation region shown in Figure 1b and the coordinate $r \in S$. The effective mass m_{eff} of the acoustic mode is given by [36,37]

$$m_{eff} = L \int_S \rho Q(r)^2 dr / \max_S (Q(r)^2), \quad (2)$$

where L is the length of the acoustic resonator along the y -direction, ρ is the material mass density of LN, and Q is the solid displacement field. Note that the acoustic mode amplitude χ_{zpf} is normalized to a single phonon occupying the acoustic resonator and the same normalization will be used in the analyses of multi-physical effects.

Secondly, the refractive index change of the optical waveguide induced by the photo-elastic effect for the X-cut TFLN is given by [26,36,37]

$$\Delta n_{PE} = \frac{\epsilon_0 n^5 \chi_{zpf}}{2} \frac{\int dr \begin{pmatrix} E_x^* & E_y^* & E_z^* \end{pmatrix} \begin{pmatrix} dB_1 & dB_6 & dB_5 \\ dB_6 & dB_2 & dB_4 \\ dB_5 & dB_4 & dB_3 \end{pmatrix} \begin{pmatrix} E_x \\ E_y \\ E_z \end{pmatrix}}{\int E^* \epsilon E dr}, \quad (3)$$

where ϵ_0 is the vacuum permittivity, E_x , E_y , E_z are the electric field components along the x -, y -, z -direction, respectively. $dB_1 \sim dB_6$ are the optical indicatrix coefficients which are closely related with the generated strain $s_1 \sim s_6$ by the SAW [26], and the transformation matrix between them should be rotated according to the X-cut Z-propagation TFLN. The transformation methods and related elasto-optic coefficients can be found in [38,39]. Finally, the electro-optic effect acting on the refractive index change of the optical waveguide (Δn_{EO}) has the same form with that of Δn_{PE} shown in Equation (3). The only difference lies in the optical indicatrix coefficients $dB_1 \sim dB_6$, which are related to the electric fields (ξ_x , ξ_y , ξ_z) of the generated SAW due to the piezoelectric effect of the TFLN [26]. Similarly, the transformation matrix also needs to be rotated for the X-cut Z-propagation TFLN and the electro-optic coefficients can be obtained from [38,39]. Therefore, the total refractive index change of the optical waveguide (Δn_{tot}) due to the combination of moving boundary effect, photo-elastic effect, and electro-optic effect for a single phonon is given by

$$\Delta n_{tot} = \Delta n_{MB} + \Delta n_{PE} + \Delta n_{EO}. \quad (4)$$

The in-cavity phonon number N_p for the input power P_{in} has the following relationship [26],

$$N_p = \frac{4\gamma_e}{\gamma^2} \frac{P_{in}}{\hbar\omega_m}, \quad P_{in} = \frac{1}{2} \frac{V_p^2}{R_{in}}, \quad (5)$$

where γ and γ_e are the decay and external coupling rates, respectively, V_p is the peak voltage of the input power, and R_{in} is the input impedance (50 Ω). To accumulate a π phase shift in the MZI structure, the phase shift relation should satisfy,

$$\frac{2\pi L}{\lambda} \Delta n_{tot} \sqrt{N_p} = \pi, \quad (6)$$

where λ is the optical wavelength ($\lambda = 1.55 \mu\text{m}$). Using Equations (5) and (6), the key modulation parameter of $V_{\pi}L$ for the proposed device is

$$V_{\pi}L = \frac{\lambda}{2\Delta n_{tot}} \sqrt{\frac{\gamma^2 \hbar \omega_m R_{in}}{2\gamma_e}}. \quad (7)$$

Thus, by enhancing the AOI through working at the higher-order TE_1 mode in the proposed on-chip AOM, the obtained Δn_{tot} could be increased effectively, leading to the reduction of $V_{\pi}L$ for the device.

3. Results

Two-dimensional cross-sectional analyses (x - z direction) are required in order to determine the key parameters of the AOM shown in Figure 1. We use the finite element simulation tool COMSOL Multiphysics to study the multi-physical coupling processes of the proposed AOM, in which the microwave electric field, mechanical field, and optical field can be obtained for analyses and optimization of the AOM structure [40]. Figure 2a illustrates the working process of the AOM from the 2D cross-sectional view. The generated SAW acts as a bridge connecting the microwave input and the optical mode index. The three multi-physical effects together induce the change in the refractive index of the optical waveguide based on the TFLN platform. Figure 2b plots the calculated strain displacement

field, piezoelectrically induced electric field, and optical electric field on the optical waveguide which is a multimode waveguide ($w = 2.1 \mu\text{m}$) supporting the higher-order TE_1 mode. Based upon these mode field distributions and the material properties of the TFLN, we can analyze and calculate the field interaction and provide effective ways to optimize the AOM structural parameters.

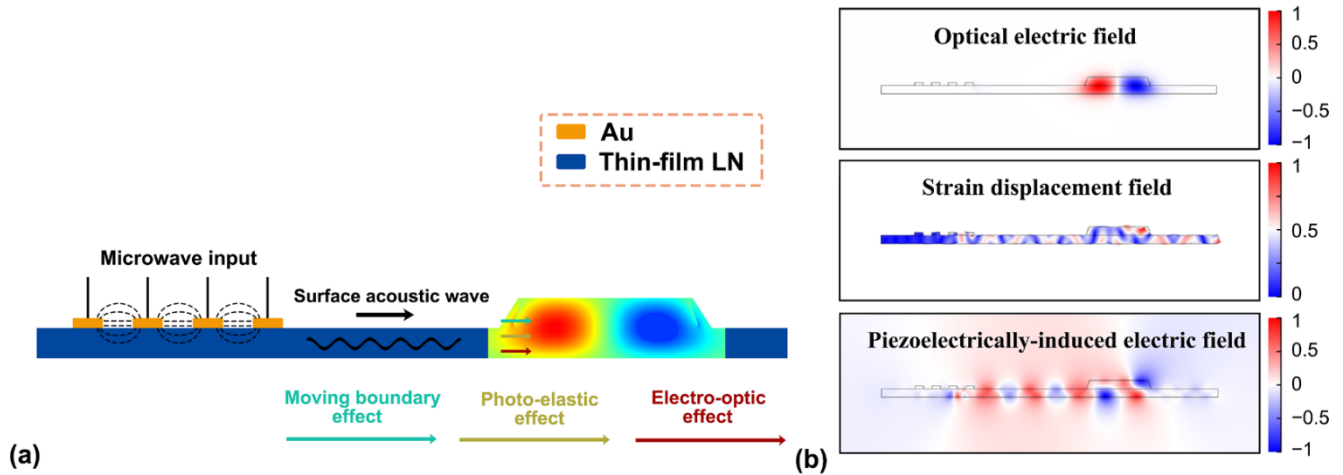


Figure 2. (a) Schematic of the working process of the proposed AOM. The microwave input and generated SAW are marked in the cross-sectional structure (x - z direction) of the AOM. Three multi-physical effects affecting the refractive index change of the optical waveguide are also plotted. (b) Mode distributions of the optical electric field, strain displacement field, and the piezoelectrically induced electric field for the same cross-sectional structure of AOM. The working wavelength is 1550 nm and the frequency of the acoustic mode is 4.08 GHz.

Next, we perform structural analyses and optimizations of the proposed on-chip AOM. Figure 3a,b show the calculated refractive index change of the optical waveguide (Δn_{tot}) induced by the AOI as a function of the gap width G between the optical waveguide and IDT, when the waveguide works at the fundamental TE_0 mode and the higher-order TE_1 mode, respectively. The single-mode and multimode waveguide widths are $w = 1.0 \mu\text{m}$ and $w = 2.1 \mu\text{m}$, respectively. From the calculations, the generated SAW has different eigenfrequencies corresponding to different strain displacement field distributions [4,25]. We use 30 frequency points around the estimated eigenfrequency of the SAW to determine the optimal microwave working frequency (which matches with the eigenfrequency of SAW) at different gap widths. For the TE_0 mode, we observe that the generated refractive index change of the optical waveguide for most of the acoustic modes is within the range from -3×10^{-10} to 3×10^{-10} for a single phonon. For the TE_1 mode, the range increases to from -5×10^{-10} to 5×10^{-10} for a single phonon. We then extract the maximum change in the refractive index of the optical waveguide ($|\Delta n_{\text{tot}}|$) at every gap width G for both the TE_0 and TE_1 modes. The results are shown in Figure 3c. The performance of the refractive index change of the TE_1 mode is clearly better than that of the TE_0 mode because of the enhanced AOI. The maximum $|\Delta n_{\text{tot}}|$ is lower than (higher than) 4×10^{-10} (6.5×10^{-10}) for the TE_0 mode (TE_1 mode) for a single phonon. The increase in the refractive index change when the optical waveguide works at the TE_1 mode will reduce the key modulation parameter $V_{\pi}L$ of the proposed AOM. From Figure 3c, we can also determine two optimum gap widths between the optical waveguide and IDT, $G = 1.7 \mu\text{m}$ and $G = 3.5 \mu\text{m}$, corresponding to the highest $|\Delta n_{\text{tot}}|$. The respective microwave working frequencies are 4.06 GHz and 4.08 GHz. In addition, since large gap width G reduces the metal absorption loss of the optical waveguide and the whole AOM device [1–5], large gaps are preferred in on-chip AOM under the same fabrication processes and requirements.

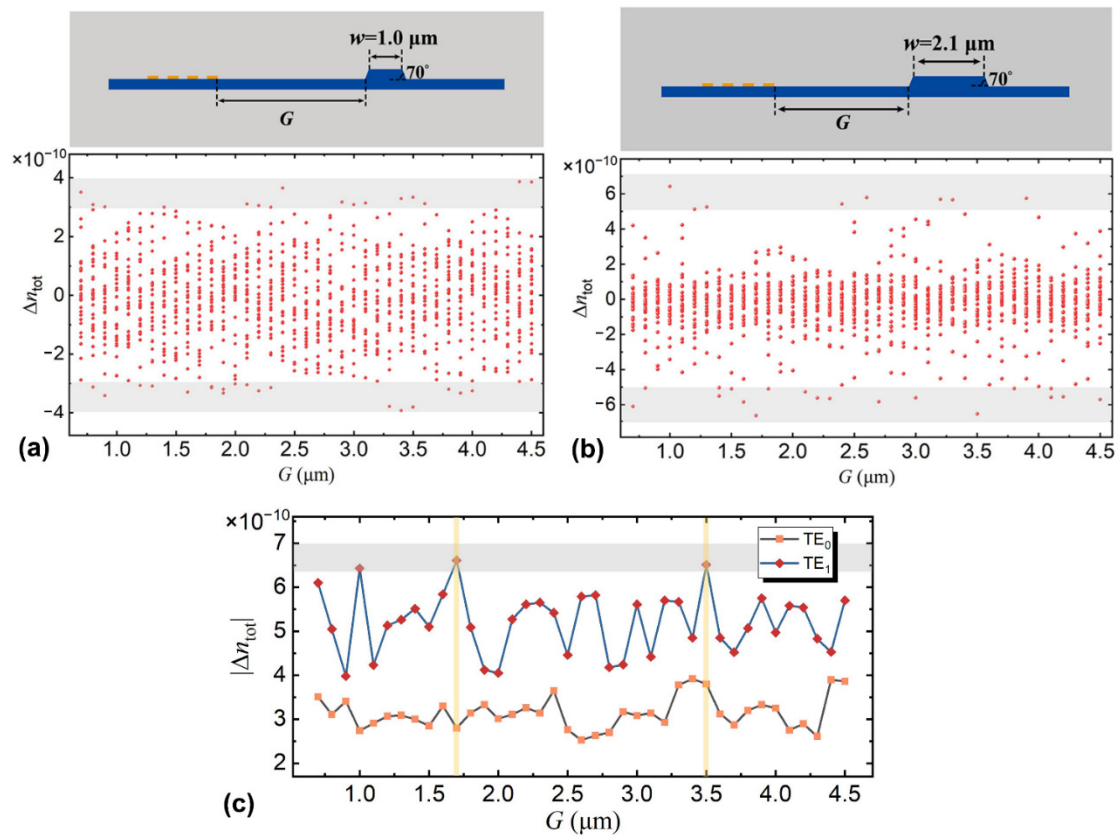


Figure 3. Refractive index change of the optical waveguide Δn_{tot} as a function of the gap width G between the optical waveguide and IDT working at the (a) fundamental TE_0 mode and (b) higher-order TE_1 mode. (c) The maximum refractive index change of the optical waveguide $|\Delta n_{\text{tot}}|$ versus the same gap width G for both the TE_0 and TE_1 mode. The results are calculated for a single phonon.

Apart from gap width G , the multimode waveguide width w is also an important parameter affecting the on-chip AOI effect. Here, we consider two cases: $G = 1.7 \mu\text{m}$ and $G = 3.5 \mu\text{m}$, and choose the maximum refractive index change of the optical waveguide $|\Delta n_{\text{tot}}|$ from the calculations at different multimode waveguide widths as shown in Figure 4. Within the calculation range from $w = 1.8$ to $2.2 \mu\text{m}$, the value of $|\Delta n_{\text{tot}}|$ increases first and then decreases. The maximum value locates at the width of $w = 2.1 \mu\text{m}$ for both of the gap width considered. The optimal waveguide width implies that the AOI effect reaches the maximum at $w = 2.1 \mu\text{m}$, a width that has also been used in the aforementioned gap width analyses. We etch two slots on both sides of the AOM to form an acoustic resonator. We use the acoustic resonance to enhance the SAW energy [25,33–35]. The resonance acoustic mode will interact further with the higher-order TE_1 mode. Thus, the acoustic resonator width should also be analyzed. Figure 5 shows the refractive index change of the optical waveguide Δn_{tot} as a function of the gap width G between the optical waveguide and IDT for different widths W_d of the acoustic resonator. The multimode waveguide width is still fixed to $w = 2.1 \mu\text{m}$ and we choose $W_d = 8, 9, 10, 11$, and $13 \mu\text{m}$. From the results, we can always find the maximum value of Δn_{tot} for different widths of the acoustic resonator by tuning the gap width G , and the obtained maximum values of $|\Delta n_{\text{tot}}|$ are all higher than 6×10^{-10} for a single phonon. The observations indicate that the field distribution of the acoustic resonator mode is closely related to the acoustic resonator width, and we need to reoptimize the position of the multimode waveguide on the TFLN for different widths W_d in order to obtain the highest AOI, which corresponds to the maximum value of $|\Delta n_{\text{tot}}|$. Moreover, through additional calculations using different acoustic resonator widths, we find that the maximum value of $|\Delta n_{\text{tot}}|$ can still be increased slightly if the width W_d is further decreased. For example, the maximum value of $|\Delta n_{\text{tot}}|$ can be even

higher than 7×10^{-10} for a single phonon if W_d is less than $8 \mu\text{m}$. However, such a small acoustic resonator width will lead to a decrease in the gap width between the optical waveguide and IDT, which will then increase the metal absorption loss of the AOM. From the above calculations, we determine the key cross-sectional dimension of the proposed AOM including the gap width G , multimode waveguide width w , and acoustic resonator width W_d , where the AOM length along the y -direction is set as $100 \mu\text{m}$ since the BOX layer below the AOM region needs to be removed [33,34]. In summary, the structural parameters of the proposed AOM can be obtained with higher AOI effect working at the higher-order TE_1 mode when compared with that working at the fundamental TE_0 mode.

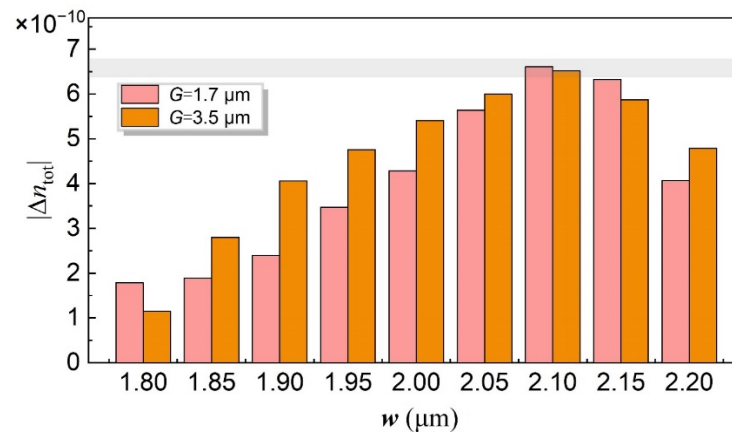


Figure 4. The maximum refractive index change of the optical waveguide $|\Delta n_{\text{tot}}|$ as a function of the waveguide width w for gap width $G = 1.7 \mu\text{m}$ and $G = 3.5 \mu\text{m}$.

Another key component of the proposed scheme is the mode converter, which realizes the conversion between the TE_0 and TE_1 mode efficiently. The mode converter is implemented by the asymmetrical directional coupler (ADC) shown in Figure 1c. From the ADC theory, the required mode conversion can be achieved via evanescent coupling under the phase matching condition [41,42]. To achieve phase matching, we calculate the mode features of the TFLN optical waveguide and make the effective index of the TE_0 mode of the single mode waveguide match with that of the TE_1 mode of the multimode waveguide. The optimized results are the single mode waveguide width $w_1 = 870 \text{ nm}$, multimode waveguide width $w = 2.1 \mu\text{m}$, and gap width between the two waveguides $d = 330 \text{ nm}$. The working wavelength is $\lambda = 1.55 \mu\text{m}$. Then we conduct transmission analyses to determine the optimum coupling length L_C [43], which can be found in Figure 6. It is noted that the highest mode transmission from the input TE_0 to output TE_1 mode is nearly 0.98 (normalized to the input power) corresponding to the coupling length $L_C = 52 \mu\text{m}$ as shown in Figure 6a. We note that the mode transmission is still higher than 0.95 even if L_C changes from 46 to $61 \mu\text{m}$, thus relaxing the fabrication tolerance of the TFLN waveguide. The transmission wavelength spectrum of the mode converter is also analyzed. From Figure 6b, the bandwidth is 123 nm for transmission higher than 0.95 (202 nm for transmission higher than 0.90). The large bandwidth can be utilized for broadband AOMs. Figure 6c shows the field evolution through the whole conversion region from the input TE_0 mode to the converted TE_1 mode and then to the output TE_0 mode, where the generated TE_1 mode is used for the AOM. The mode patterns of the input TE_0 mode and the converted TE_1 mode are also shown in the insets. We find that the converted TE_1 mode has a high mode purity and low mode crosstalk, contributing to the efficient operation of the AOM working at the higher-order TE_1 mode. In summary, the key structures of the AOM and the mode converter have been obtained. The rest are typical MZI structure shown in Figure 1a, the waveguide width of which is 870 nm .

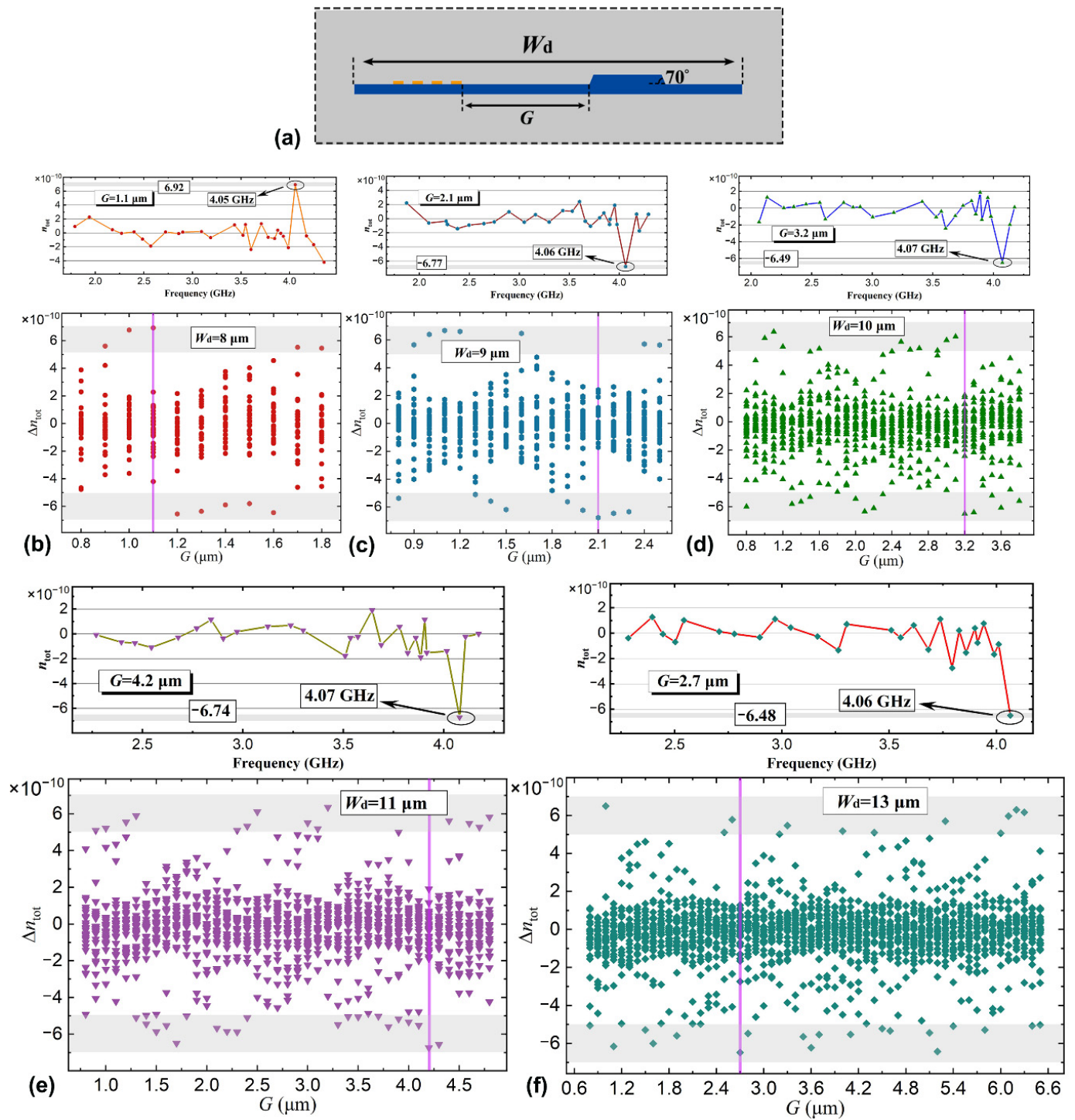


Figure 5. (a) A 2D cross section of the acoustic resonator. Its width is W_d . The calculated refractive index change of the optical waveguide Δn_{tot} versus the gap width G between the optical waveguide and IDT. The acoustic resonator widths are $W_d =$ (b) 8, (c) 9, (d) 10, (e) 11, and (f) 13 μm , respectively. Vertical lines show the chosen optimum gap widths. The frequency distributions are illustrated in the upper diagram.

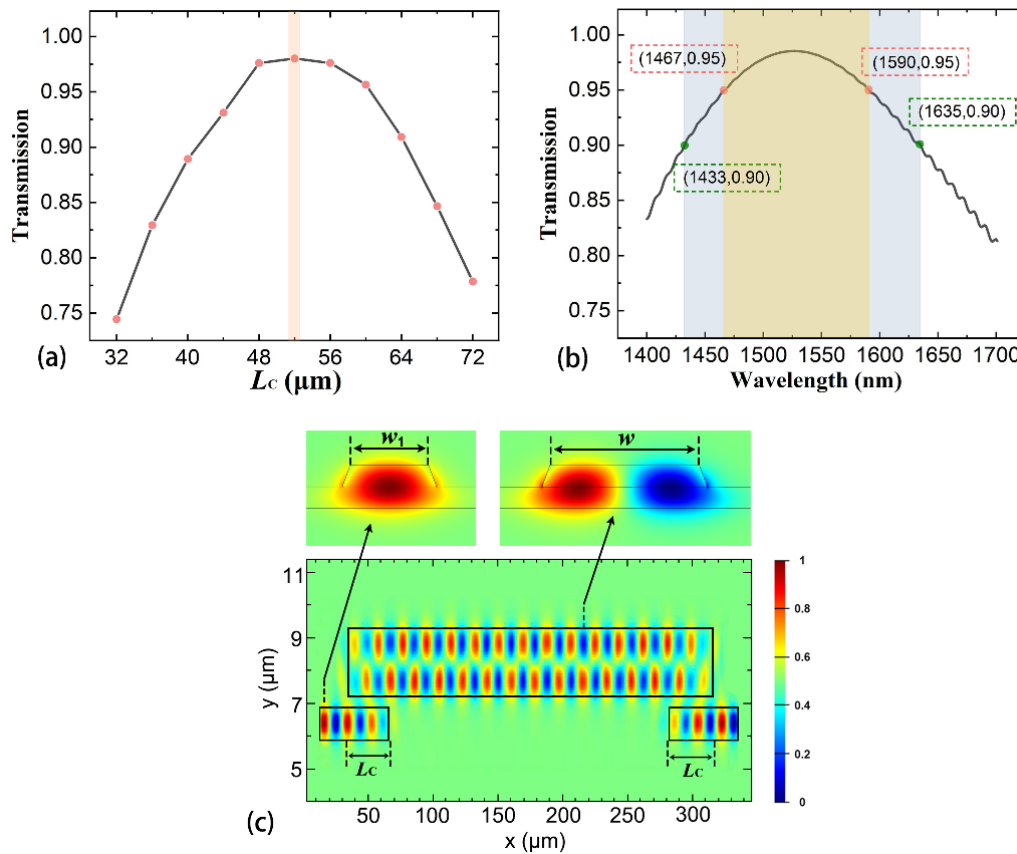


Figure 6. (a) Mode transmission from the input TE_0 to output TE_1 mode as a function of its coupling length L_c . (b) Transmission wavelength spectrum for the mode converter. The optical bandwidths for transmission higher than 0.95 and 0.90 are marked with light yellow and light gray regions, respectively. (c) Electric field evolution through the whole conversion region from the input TE_0 mode to the converted TE_1 mode and then to the output TE_0 mode. The mode patterns of the input TE_0 mode and the converted TE_1 mode are shown in the insets. The coupling length $L_c = 52 \mu\text{m}$.

4. Discussion

The device fabrication process can be divided into three steps; they are (1) define the TFLN waveguide structure, (2) fabricate the IDT electrode on the TFLN, and (3) open the acoustic resonator slot and remove the BOX layer below the AOM region. We can start from the X-cut TFLN wafer with a 600 nm-thick top LN layer. First, the designed optical waveguide structure of the AOM is patterned and etched on the TFLN wafer using E-beam lithography (EBL) and reactive ion etching (RIE) [2–5,25], where the waveguide widths ($w = 2.1 \mu\text{m}$, $w_1 = 870 \text{ nm}$), gap ($d = 330 \text{ nm}$), and etching depth ($h_1 = 300 \text{ nm}$) should be well controlled. Second, we use typical metal lift-off process to fabricate the IDT electrode [2–5,25], where the electrode width ($a = 300 \text{ nm}$), gap ($b = 300 \text{ nm}$), and thickness (100 nm) need to be satisfied. Third, two rectangular slots on both sides of the AOM are etched on the slab layer with etching depth $h_2 = 300 \text{ nm}$ to form the acoustic resonator. Finally, we employ BOX etchant contact with the BOX layer and then remove it through two completely etched slots of the TFLN layer [33,34]. For these fabrication steps, we calculated the refractive index change of the optical waveguide Δn_{tot} as functions of the IDT electrode thickness and waveguide etching depth h_1 . We note that no obvious variation of Δn_{tot} is observed as the IDT electrode thickness changes from 80 to 120 nm. In contrast, the waveguide etching depth variation has a stronger effect on Δn_{tot} since it is directly related to the mode features of the generated SAW and the optical waveguide, leading to variation of the AOI effect. Therefore, the waveguide etching depth ($h_1 = 300 \text{ nm}$) should be carefully controlled during device fabrication process.

Finally, we calculate the key modulation parameter $V_{\pi}L$ for the proposed device due to refractive index change of the optical waveguide where Equation (7) is used to estimate the value. The AOM length along the y -direction is chosen to be 100 μm and the beam length of the MZI structure is 500 μm . The typical Q factor of the acoustic resonator $Q_m = 2000$, $\gamma = \omega_m/Q_m$ and $\gamma_e/\gamma = 0.15$ (from experimental results) are used in the following calculations [26]. Table 1 lists the calculation results at the TE₀ and TE₁ modes. The value of Δn_{tot} is chosen as the maximum one generated by the specific acoustic mode frequency chosen from various acoustic mode frequencies for every device structure mentioned above. We find that the use of the higher-order TE₁ mode reduces the key modulation parameter $V_{\pi}L$ for the proposed AOM. The minimum value $V_{\pi}L$ is ~ 0.0084 V·cm, which is obviously lower than previous reports [25–29]. Figure 7 shows the refractive index change Δn_{tot} of the waveguide versus the slant angle of the TFLN waveguide sidewall. Other waveguide parameters are the same as that in Figure 3b, where $G = 3.5$ μm . Note that the allowable slant angle can be varied from 64° to 70°, while keeping $|\Delta n_{\text{tot}}|$ higher than 6.5×10^{-10} for a single phonon. Such relatively large tolerance is useful in the etching process of the TFLN waveguide. Thus, the AOI effect is enhanced by using the higher-order TE₁ mode, leading to the performance improvement of on-chip AOM.

Table 1. Comparison of the AOM effect working at TE₀ and TE₁ mode for different device structures.

Optical Waveguide Mode	w (μm)	G (μm)	W_d (μm)	Acoustic Mode Frequency (GHz)	$ \Delta n_{\text{tot}} $ $\times 10^{-10}$	$V_{\pi}L$ (V·cm)
TE ₀	1.0	3.4	12	3.86	3.72	0.01498
TE ₁	2.1	1.7	12	4.06	6.61	0.00886
TE ₁	2.1	3.5	12	4.08	6.51	0.00904
TE ₁	2.1	1.1	8	4.05	6.92	0.00845
TE ₁	2.1	2.1	9	4.06	6.77	0.00866
TE ₁	2.1	3.2	10	4.07	6.49	0.00905
TE ₁	2.1	4.2	11	4.07	6.74	0.00872
TE ₁	2.1	2.7	13	4.06	6.48	0.00904

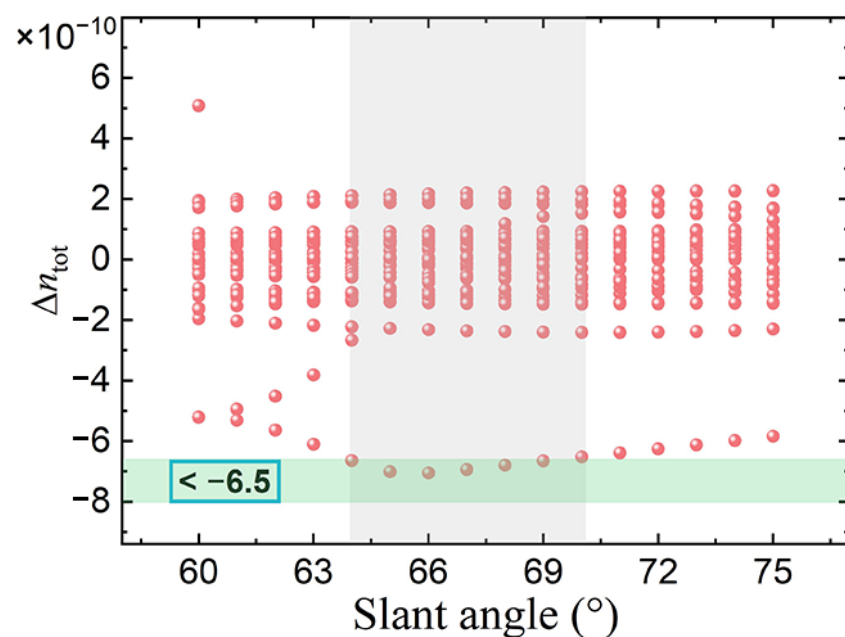


Figure 7. The refractive index change of the optical waveguide Δn_{tot} as a function of the slant angle of the TFLN waveguide sidewall. Other structural parameters are the same as that in Figure 3b and $G = 3.5$ μm .

5. Conclusions

In conclusion, we have proposed an on-chip AOM based on the typical TFLN platform, in which the optical waveguide is a multimode waveguide supporting the higher-order TE_1 mode instead of the commonly used fundamental TE_0 mode. To analyze the multiple physical field features and determine the optimum structural parameters of the proposed AOM, multi-physical field coupling analyses were carried out by considering the photo-elastic effect, moving boundary effect, and electro-optic effect. We observed that the change of the refractive index of the optical waveguide increases ($>6.5 \times 10^{-10}$ for a single phonon) because of the enhanced AOI effect. We then added the proposed AOM structure to an MZI circuit to form an MZI-type AOM, where the mode converters between the TE_0 and TE_1 mode have been designed and embedded at both sides of the AOM. From the results, the key half-wave-voltage-length product $V_{\pi}L$ is calculated to be less than $0.01 \text{ V}\cdot\text{cm}$, which can be used for low-power modulation. In addition, the metal absorption loss is quite low for the proposed AOM since the electrode can be placed far from the optical waveguide when compared to typical EOM structures in which the electrode must be placed close to the optical waveguide. The proposed device would contribute to the development of on-chip high-performance multimode AOM.

Author Contributions: Conceptualization, Y.X.; methodology, Y.Y., Y.X., D.H., and F.L.; investigation, Y.Y., Y.X., Y.D., and B.Z.; writing—original draft preparation, Y.Y. and Y.X.; writing—review and editing, all authors; supervision, Y.X., D.H., F.L., Y.N., and P.K.A.W.; project administration, Y.X., D.H., F.L., and P.K.A.W. All authors have read and agreed to the published version of the manuscript.

Funding: This research was funded by the National Key R&D Program of China, grant number 2019YFB1803904, Research Grant Council of Hong Kong SAR, grant number PolyU152241/18E, Natural Science Foundation of Jiangsu Province, grant number BK20200592, and Fundamental Research Funds for the Central Universities, grant number JUSRP12024.

Institutional Review Board Statement: Not applicable.

Informed Consent Statement: Not applicable.

Data Availability Statement: The data that support the findings of this study are available from the corresponding author upon reasonable request.

Conflicts of Interest: The authors declare no conflict of interest.

References

1. Zhu, D.; Shao, L.; Yu, M.; Cheng, R.; Desiatov, B.; Xin, C.J.; Hu, Y.; Holzgrafe, J.; Ghosh, S.; Shams-Ansari, A.; et al. Integrated photonics on thin-film lithium niobate. *Adv. Opt. Photon.* **2021**, *13*, 242–352. [\[CrossRef\]](#)
2. Sarabalis, C.J.; McKenna, T.P.; Patel, R.N.; Laer, R.V.; Safavi-Naeini, A.H. Acousto-optic modulation in lithium niobate on sapphire. *APL Photon.* **2020**, *5*, 086104. [\[CrossRef\]](#)
3. Hassanien, A.E.; Link, S.; Yang, Y.; Chow, E.; Goddard, L.L.; Gong, S. Efficient and wideband acousto-optic modulation on thin-film lithium niobate for microwave-to-photon conversion. *Photon. Res.* **2021**, *9*, 1182–1190. [\[CrossRef\]](#)
4. Tadesse, S.A.; Li, M. Sub-optical wavelength acoustic wave modulation of integrated photonic resonators at microwave frequencies. *Nat. Commun.* **2014**, *5*, 5402. [\[CrossRef\]](#)
5. Kittlaus, E.A.; Jones, W.M.; Rakich, P.T.; Otterstrom, N.T.; Muller, R.E.; Rais-Zadeh, M. Electrically driven acousto-optics and broadband non-reciprocity in silicon photonics. *Nat. Photon.* **2021**, *15*, 43–52. [\[CrossRef\]](#)
6. Wang, C.; Zhang, M.; Chen, X.; Bertrand, M.; Shams-Ansari, A.; Chandrasekhar, S.; Winzer, P.; Lončar, M. Integrated lithium niobate electro-optic modulators operating at CMOS-compatible voltages. *Nature* **2018**, *562*, 101–104. [\[CrossRef\]](#) [\[PubMed\]](#)
7. He, M.; Xu, M.; Ren, Y.; Jian, J.; Ruan, Z.; Xu, Y.; Gao, S.; Sun, S.; Wen, X.; Zhou, L.; et al. High-performance hybrid silicon and lithium niobate Mach–Zehnder modulators for 100 Gbit s^{-1} and beyond. *Nat. Photon.* **2019**, *13*, 359–364. [\[CrossRef\]](#)
8. Sinatkas, G.; Christopoulos, T.; Tsilipakos, O.; Kriezis, E.E. Electro-optic modulation in integrated photonics. *J. Appl. Phys.* **2021**, *130*, 010901. [\[CrossRef\]](#)
9. Zhang, M.; Wang, C.; Kharel, P.; Zhu, D.; Lončar, M. Integrated lithium niobate electro-optic modulators: When performance meets scalability. *Optica* **2021**, *8*, 652–667. [\[CrossRef\]](#)
10. Li, M.; Ling, J.; He, Y.; Javid, U.A.; Xue, S.; Lin, Q. Lithium niobate photonic-crystal electro-optic modulator. *Nat. Commun.* **2020**, *11*, 4123. [\[CrossRef\]](#) [\[PubMed\]](#)

11. Bochmann, J.; Vainsencher, A.; Awschalom, D.D.; Cleland, A.N. Nanomechanical coupling between microwave and optical photons. *Nat. Phys.* **2013**, *9*, 712–716. [[CrossRef](#)]
12. Li, N.; Ho, C.P.; Zhu, S.; Fu, Y.H.; Zhu, Y.; Lee, L.Y.T. Aluminium nitride integrated photonics: A review. *Nanophoton.* **2021**, *10*, 2347–2387. [[CrossRef](#)]
13. Ramp, H.; Hauer, B.D.; Balram, K.C.; Clark, T.J.; Srinivasan, K.; Davis, J.P. Elimination of thermomechanical noise in piezoelectric optomechanical crystals. *Phys. Rev. Lett.* **2019**, *123*, 093603. [[CrossRef](#)] [[PubMed](#)]
14. Forsch, M.; Stockill, R.; Wallucks, A.; Marinković, I.; Gärtner, C.; Norte, R.A.; Otten, F.; Fiore, A.; Srinivasan, K.; Gröblacher, S. Microwave-to-optics conversion using a mechanical oscillator in its quantum ground state. *Nat. Phys.* **2020**, *16*, 69–74. [[CrossRef](#)] [[PubMed](#)]
15. Stockill, R.; Forsch, M.; Beaudoin, G.; Pantzas, K.; Sagnes, I.; Braive, R.; Gröblacher, S. Gallium phosphide as a piezoelectric platform for quantum optomechanics. *Phys. Rev. Lett.* **2019**, *123*, 163602. [[CrossRef](#)]
16. Stockill, R.; Forsch, M.; Hijazi, F.; Beaudoin, G.; Pantzas, K.; Sagnes, I.; Braive, R.; Gröblacher, S. Ultra-low-noise microwave to optics conversion in gallium phosphide. *arXiv* **2021**, arXiv:2107.04433.
17. Katzman, M.; Munk, D.; Priel, M.; Grunwald, E.; Hen, M.; Inbar, N.; Feldberg, M.; Sharabani, T.; Zektzer, R.; Bashan, G.; et al. Surface acoustic microwave photonic filters in standard silicon-on-insulator. *Optica* **2021**, *8*, 697–707. [[CrossRef](#)]
18. Munk, D.; Katzman, M.; Hen, M.; Priel, M.; Feldberg, M.; Sharabani, T.; Levy, S.; Bergman, A.; Zadok, A. Surface acoustic wave photonic devices in silicon on insulator. *Nat. Commun.* **2019**, *10*, 4214. [[CrossRef](#)] [[PubMed](#)]
19. Lin, J.; Bo, F.; Cheng, Y.; Xu, J. Advances in on-chip photonic devices based on lithium niobate on insulator. *Photon. Res.* **2020**, *8*, 1910–1936. [[CrossRef](#)]
20. Honardoost, A.; Abdelsalam, K.; Fathpour, S. Rejuvenating a versatile photonic material: Thin-film lithium niobate. *Laser Photon. Rev.* **2020**, *14*, 2000088. [[CrossRef](#)]
21. Jia, Y.; Wang, L.; Chen, F. Ion-cut lithium niobate on insulator technology: Recent advances and perspective. *Appl. Phys. Rev.* **2021**, *8*, 011307. [[CrossRef](#)]
22. Boes, A.; Corcoran, B.; Chang, L.; Bowers, J.; Mitchell, A. Status and potential of lithium niobate on insulator (LNOI) for photonic integrated circuits. *Laser Photon. Rev.* **2018**, *12*, 1700256. [[CrossRef](#)]
23. Qi, Y.; Li, Y. Integrated lithium niobate photonics. *Nanophoton* **2020**, *9*, 1287–1320. [[CrossRef](#)]
24. Luke, K.; Kharel, P.; Reimer, C.; He, L.; Loncar, M.; Zhang, M. Wafer-scale low-loss lithium niobate photonic integrated circuits. *Opt. Express* **2020**, *28*, 24452–24458. [[CrossRef](#)] [[PubMed](#)]
25. Cai, L.; Mahmoud, A.; Khan, M.; Mahmoud, M.; Mukherjee, T.; Bain, J.; Piazza, G. Acousto-optical modulation of thin film lithium niobate waveguide devices. *Photon. Res.* **2019**, *7*, 1003–1013. [[CrossRef](#)]
26. Shao, L.; Yu, M.; Maity, S.; Sinclair, N.; Zheng, L.; Chia, C.; Shams-Ansari, A.; Wang, C.; Zhang, M.; Lai, K.; et al. Microwave-to-optical conversion using lithium niobate thin-film acoustic resonators. *Optica* **2019**, *6*, 1498–1505. [[CrossRef](#)]
27. Huang, X.; Liu, Y.; Li, Z.; Guan, H.; Wei, Q.; Tan, M.; Li, Z. 40 GHz high-efficiency Michelson interferometer modulator on a silicon-rich nitride and thin-film lithium niobate hybrid platform. *Opt. Lett.* **2021**, *46*, 2811–2814. [[CrossRef](#)] [[PubMed](#)]
28. Xu, M.; Chen, W.; He, M.; Wen, X.; Ruan, Z.; Xu, J.; Chen, L.; Liu, L.; Yu, S.; Cai, X. Michelson interferometer modulator based on hybrid silicon and lithium niobate platform. *APL Photon.* **2019**, *4*, 100802. [[CrossRef](#)]
29. Liu, Y.; Li, H.; Liu, J.; Tan, S.; Lu, Q.; Guo, W. Low V_π thin-film lithium niobate modulator fabricated with photolithography. *Opt. Express* **2021**, *29*, 6320–6329. [[CrossRef](#)] [[PubMed](#)]
30. Ma, X.; Zhuang, C.; Zeng, R.; Coleman, J.J.; Zhou, W. Polarization-independent one-dimensional grating coupler design on hybrid silicon/LNOI platform. *Opt. Express* **2020**, *28*, 17113–17121. [[CrossRef](#)]
31. Han, X.; Jiang, Y.; Frigg, A.; Xiao, H.; Zhang, P.; Boes, A.; Nguyen, T.G.; Yang, J.; Ren, G.; Su, Y.; et al. Single-step etched grating couplers for silicon nitride loaded lithium niobate on insulator platform. *APL Photon.* **2021**, *6*, 086108. [[CrossRef](#)]
32. Yu, Z.; Sun, X. Acousto-optic modulation of photonic bound state in the continuum. *Light. Sci. Appl.* **2020**, *9*, 1. [[CrossRef](#)] [[PubMed](#)]
33. Balram, K.C.; Davanço, M.I.; Ilic, B.R.; Kyhm, J.H.; Song, J.D.; Srinivasan, K. Acousto-optic modulation and optoacoustic gating in piezo-optomechanical circuits. *Phys. Rev. Appl.* **2017**, *7*, 024008. [[CrossRef](#)] [[PubMed](#)]
34. Fang, K.; Matheny, M.H.; Luan, X.; Painter, O. Optical transduction and routing of microwave phonons in cavity-optomechanical circuits. *Nat. Photon.* **2016**, *10*, 489–496. [[CrossRef](#)]
35. Jiang, W.; Sarabalis, C.J.; Dahmani, Y.D.; Patel, R.N.; Mayor, F.M.; McKenna, T.P.; Laer, R.V.; Safavi-Naeini, A.H. Efficient bidirectional piezo-optomechanical transduction between microwave and optical frequency. *Nat. Commun.* **2020**, *11*, 1166. [[CrossRef](#)] [[PubMed](#)]
36. Li, Y.; Cui, K.; Feng, X.; Huang, Y.; Huang, Z.; Liu, F.; Zhang, W. Optomechanical crystal nanobeam cavity with high optomechanical coupling rate. *J. Opt.* **2015**, *17*, 045001. [[CrossRef](#)]
37. Chan, J.; Safavi-Naeini, A.H.; Hill, J.T.; Meenehan, S.; Painter, S. Optimized optomechanical crystal cavity with acoustic radiation shield. *Appl. Phys. Lett.* **2012**, *101*, 081115. [[CrossRef](#)]
38. Weis, R.S.; Gaylord, T.K. Lithium niobate: Summary of physical properties and crystal structure. *Appl. Phys. A* **1985**, *37*, 191–203. [[CrossRef](#)]
39. Wang, Y.; Jiang, Y. Crystal orientation dependence of piezoelectric properties in LiNbO_3 and LiTaO_3 . *Opt. Mat.* **2003**, *23*, 403–408. [[CrossRef](#)]

-
40. COMSOL Multiphysics. Available online: <https://www.comsol.com> (accessed on 20 August 2021).
 41. Dai, D.; Wang, S. Asymmetric directional couplers based on silicon nanophotonic waveguides and applications. *Front. Optoelectron.* **2016**, *9*, 450–465. [[CrossRef](#)]
 42. Xu, H.; Shi, Y. On-chip silicon TE-pass polarizer based on asymmetrical directional couplers. *IEEE Photon. Technol. Lett.* **2017**, *29*, 861–864. [[CrossRef](#)]
 43. Sullivan, D.M. *Electromagnetic Simulation Using the FDTD Method*; IEEE Press: Piscataway Township, NJ, USA, 2000.